

Nyquist-Sampling and Degrees of Freedom of Electromagnetic Fields

Andrea Pizzo, *Member, IEEE*, Andrea de Jesus Torres, *Student Member, IEEE*,
Luca Sanguinetti, *Senior Member, IEEE*, Thomas L. Marzetta, *Life Fellow, IEEE*

Abstract—A signal-space approach is presented to study the Nyquist sampling and number of degrees of freedom of an electromagnetic field under arbitrary propagation conditions. Conventional signal processing tools such as the multidimensional sampling theorem and Fourier theory are used to build a linear system theoretic interpretation of electromagnetic wave propagations and revisit classical electromagnetic theory results, e.g., bandlimited property of an electromagnetic field, from a signal processing perspective. Scalar electromagnetic fields are considered for simplicity, which physically correspond to acoustic propagation in general or electromagnetic propagation under certain conditions. The developed approach is extended to study ensembles of a stationary random electromagnetic field that is representative of different propagation conditions.

Index Terms—Multidimensional sampling theorem, Nyquist sampling, degrees of freedom, field reconstruction, Helmholtz equation, Fourier spectral representation.

I. INTRODUCTION

The Kotelnikov-Shannon-Whittaker sampling theorem [2]–[4] states that any squared-integrable signal of finite bandwidth Ω/π Hz, i.e., $e(t) \in \mathcal{B}_\Omega$, can be perfectly reconstructed from its samples taken at equally spaced $Q^* = \pi/\Omega$ seconds apart by the reconstruction formula (also called cardinal series)

$$e(t) = \sum_{n \in \mathbb{Z}} e(nQ^*) f_\Omega(t - nQ^*) \quad (1)$$

where $f_\Omega(t) = \text{sinc}(t/Q^*)$. Orthonormality is a fundamental property of the reconstruction sinc-functions, which allows to geometrically interpret the samples as coordinates of a basis set of functions [2]. In general, $e(t)$ may not be bandlimited, and an ideal low-pass filtering operation is required prior to sampling with reduced reconstruction accuracy [5].

The generalization of the sampling theorem to a finite bandwidth multivariate signal (or field) $e(\mathbf{r})$ with $\mathbf{r} \in \mathbb{R}^n$ is known as multidimensional sampling theorem [6]–[9]. Its application requires an accurate description of $e(\mathbf{r})$ in the spectral domain, which strongly depends on its physical nature. For communication theorists, the class of three-dimensional (3D) electromagnetic fields is of great interest as they allow the wireless transfer of information from one point to another [10]. A field of this sort generates an uncountably infinite number of samples per unit of space in the form of a continuous-space physical process. However, practical systems

Part of this work was presented at the IEEE 21st International Workshop on Signal Processing Advances in Wireless Communications (SPAWC), Georgia, US, 2020 [1]. A. Pizzo, A. d. J. Torres, and L. Sanguinetti are with the Dipartimento di Ingegneria dell’Informazione, University of Pisa, 56122 Pisa, Italy (e-mail: andrea.pizzo@ing.unipi.it; andrea.dejesustorres@phd.unipi.it; luca.sanguinetti@unipi.it). T. L. Marzetta is with the Department of Electrical and Computer Engineering, Tandon School of Engineering, 11201 Brooklyn, NY (e-mail: tom.marzetta@nyu.edu).

are inevitably constrained by a finite precision, which requires an information-lossless finite description of the field [11].

A. Contributions

The emergence of metamaterials enables a full manipulation of the propagation environment surrounding the user, which may represent a major paradigm change in wireless communications systems in terms of data rate, coverage, and enhanced security/privacy [12]–[15]. Once deployed, metamaterials can turn any man-made structure like building and wall into a smart surface [15]. However, full exploitation of the potentialities offered by smart surfaces is only possible via an understanding of the electromagnetic wave propagation phenomena [10], [11].

Motivated by these considerations, this paper revisits the Nyquist sampling theory for scalar electromagnetic fields [16]. Unlike [17], [18], a signal processing interpretation of wave propagation under arbitrary scattering is provided, based on which 3D wireless propagation can be modeled as a two-dimensional (2D) linear and space-invariant (LSI) system with circularly-bandlimited and low-pass filter behaviour.

Physics-driven approaches similar to the one used in this paper are found in [19]–[21], where the number of degrees of freedom (DoF) that can be extracted via electromagnetic fields from a region of space with spherical symmetry is computed. Differently, we consider rectangular region of spaces and carry our calculation in Cartesian coordinates by leveraging the connection with Fourier theory [22]–[26]. In addition, we connect the DoF result with the Nyquist sampling and field reconstruction problem. Some of our results also appeared in [12] under isotropic scattering only. We provide a better understanding of these results via a signal processing approach and generalizes [12] to arbitrary propagation conditions.

In order to abstract from a particular configuration of the scatterers, we extend the analysis to ensembles of stationary random electromagnetic fields [23]–[26]. We show that the results obtained for a deterministic field can be extended to every ensemble of a random field after replacing the field’s spectrum with its power spectral density and must be interpreted on average. The reconstruction via cardinal series is still possible and provides us with the best linear interpolator in the mean-squared error sense [8], [9].

B. Outline of the Paper and Notation

The remainder of this paper is organized as follows. In Section II, we review the sampling theorem for time-domain signals and put much emphasis on the Nyquist sampling, reconstruction, and number of DoF. In Section III, we provide

a spectral characterization of the class of 3D electromagnetic fields. This is first used in Section IV to solve the Nyquist sampling and reconstruction problem and later in Section V to compute the DoF. The generalization of the developed framework to ensembles of stationary random electromagnetic fields is given in Section VI. Some numerical results are given in Section VII to corroborate the developed theory. Some conclusions are drawn in Section VIII.

We use lower (upper) case letters for spatial (spectral) entities. Boldfaced letters indicate vectors and matrices. Sets \mathcal{X} are indicated by calligraphic letters and have Lebesgue measure $m(\mathcal{X})$. $\mathbb{1}_{\mathcal{X}}(x)$ is the indicator function. $\text{sinc}(x) = \sin(\pi x)/(\pi x)$ is the sinc function. $\text{jinc}(x) = J_1(x)/x$ is the jinc function where $J_1(x)$ denotes the Bessel function of the first kind with order 1. $\mathbb{E}\{\cdot\}$ denotes the expectation operator. \mathbb{R}^n and \mathbb{Z}^n are the n -dimensional spaces of real-valued and integer numbers. A general point $(\mathbf{r}, z) \in \mathbb{R}^3$ is described by its Cartesian coordinates (x, y, z) . $\|\mathbf{r}\|$ indicates the Euclidean norm of a vector \mathbf{r} . $\nabla_{\mathbf{r}}^2 = \frac{\partial^2}{\partial x^2} + \frac{\partial^2}{\partial y^2}$ is the Laplacian operator in \mathbb{R}^2 . The superscripts τ , $^{-1}$, and $^{1/2}$ stand for transposition, inverse, and matrix square root, respectively. \mathbf{I}_n is the $n \times n$ identity matrix. We denote $\text{diag}(\mathbf{x})$ the diagonal matrix with elements from \mathbf{x} . $\det(\mathbf{X})$ is the determinant of \mathbf{X} . $\lceil x \rceil$ denotes the least integer greater than or equal to x .

II. PRELIMINARIES

To make the paper self-contained, we briefly review the sampling theorem and its implications for time-domain signals. This is preparatory for studying spatial electromagnetic fields.

Let $e(t)$ be a baseband continuous-time signal of infinite time duration with centered spectrum $E(\omega)$.¹ The sampled signal $e_s(t)$ obtained from the samples $\{e(nQ)\}$ of $e(t)$, taken at equally spaced Q seconds apart, is

$$e_s(t) = \sum_{n \in \mathbb{Z}} e(nQ) \delta(t - nQ). \quad (2)$$

The Fourier transform of $e_s(t)$ is [6, Sec. 3]

$$E_s(\omega) = \sum_{n \in \mathbb{Z}} e(nQ) e^{-j\omega nQ} \quad (3)$$

$$= \frac{1}{Q} \sum_{\ell \in \mathbb{Z}} E(\omega - \ell P) \quad (4)$$

where the frequency replication period P is such that

$$PQ = 2\pi. \quad (5)$$

Suppose $e(t) \in \mathcal{B}_\Omega$, i.e., it has finite bandwidth Ω/π (in Hz). From (4), the frequency replicas of $E(\omega)$ do not overlap, (i.e., no *aliasing* occurs) when $P \geq 2\Omega$ or, equivalently, $Q \leq \pi/\Omega$. The Nyquist sampling interval is

$$Q^* = \pi/\Omega \quad (6)$$

and the Nyquist sampling rate $\mu = 1/Q^*$ (in samples/s) provides the minimum number of samples per unit of time.

¹A centered spectrum can always be obtained by opportunely choosing the frequency of the bandpass downconversion.

Under Nyquist sampling, $E(\omega)$ can be perfectly retrieved by low-pass filtering $E_s(\omega)$ in (4), i.e.,

$$E(\omega) = E_s(\omega) (Q^* \mathbb{1}_{|\omega| \leq \Omega}(\omega)). \quad (7)$$

By taking the inverse Fourier transform of (7) with $E_s(\omega)$ given by (3) yields the reconstruction formula in (1) [6, Sec. 3], [2]. The interpolating sinc-function does not depend on the spectral characteristics of $E(\omega)$, but only on the Lebesgue measure of its support, i.e., the signal's bandwidth Ω .

In principle, $e(t) \in \mathcal{B}_\Omega$ may span an infinite-dimensional function space and a countably-infinite number of samples is needed to specify the signal exactly. Nevertheless, \mathcal{B}_Ω has an effective dimension that allows us to truncate (1) up to a countable number of samples for any given accuracy. The minimum number of such samples defines the DoF of $e(t)$ [27, Sec. 2]. Within a time interval $t \in [0, T]$ of duration T , since there are $1/Q^*$ samples/s, we have a total of [27, Eq. (2.14)]

$$\text{dof}_\Omega = \left\lceil \frac{\Omega T}{\pi} \right\rceil \quad (8)$$

significant samples in the interval [2]. The implication of (8) is that only a finite number of samples carries the information contained in the signal and can be used to reconstruct it. The reconstruction error becomes negligible as $\Omega T \rightarrow \infty$ [27, Sec. 2]. Oversampling, i.e., sampling above the Nyquist rate, does not create any additional DoF and adds an insignificant contribution to the signal's reconstruction.

III. SPECTRAL CHARACTERIZATION OF AN ELECTROMAGNETIC FIELD

Based on the sampling theorem, any signal $e(t) \in \mathcal{B}_\Omega$ can approximately be identified by a countable number of samples taken at Nyquist rate, which is univocally determined by the bandwidth of its spectrum. The generalization of the sampling theorem to a 3D electromagnetic field requires a spectral characterization of the field itself. This is addressed in this section under the assumption that the field propagates in a 3D homogeneous and isotropic medium and it is generated by some arbitrary configuration of scatterers confined in the half-space $z < 0$. Hence, in any spatial region within $z \geq 0$, the electromagnetic wave propagation is source-free. Under these conditions, the Maxwell's equations reduce to the vector homogeneous Helmholtz equations in the frequency domain [16, Eq. (1.2.20)]

$$\left(\nabla_{\mathbf{r}}^2 + \frac{\partial^2}{\partial z^2} \right) \mathbf{e}(\mathbf{r}, z) + \kappa^2 \mathbf{e}(\mathbf{r}, z) = 0 \quad (9)$$

where $\mathbf{e}(\mathbf{r}, z)$ with $\mathbf{r} = (x, y) \in \mathbb{R}^2$ can be either the electric or magnetic vector fields and $\kappa = 2\pi/\lambda$ is the real-valued wavenumber with λ being the wavelength. We do our analysis in Cartesian coordinates, i.e., $\mathbf{e}(\mathbf{r}, z) = \hat{\mathbf{x}}e_x + \hat{\mathbf{y}}e_y + \hat{\mathbf{z}}e_z$. In this case, (9) can be addressed independently² along any of the three coordinates via the scalar homogeneous Helmholtz equation, which is discussed next.³

²Note that the separability does not hold in spherical coordinates where (9) must be solved in vector form [16, Sec. 1.2].

³Other physical phenomena can be described using the scalar homogeneous Helmholtz equation such as acoustic waves propagation [21], [28].

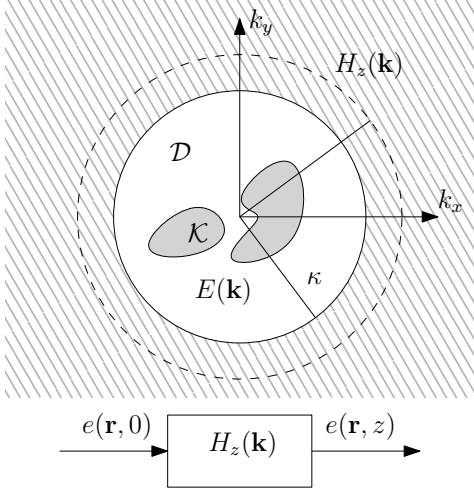


Fig. 1. Wave propagation in a 3D homogeneous, isotropic, and source-free medium can be modelled as an LSI circularly-bandlimited low-pass filter of bandwidth $m(D)$.

A. Scalar Homogeneous Helmholtz Equation

Without loss of generality, we denote with $e(\mathbf{r}, z)$ either e_x , e_y or e_z . This field obeys the scalar homogeneous Helmholtz equation [16, Eq. (1.2.21)]

$$\left(\nabla_{\mathbf{r}}^2 + \frac{\partial^2}{\partial z^2}\right) e(\mathbf{r}, z) + \kappa^2 e(\mathbf{r}, z) = 0. \quad (10)$$

The 2D spatial Fourier transform of (10), taken with respect to \mathbf{r} , yields

$$\frac{\partial^2}{\partial z^2} E(\mathbf{k}, z) + (\kappa^2 - \|\mathbf{k}\|^2) E(\mathbf{k}, z) = 0 \quad (11)$$

where $\mathbf{k} = (k_x, k_y) \in \mathbb{R}^2$ are the 2D Cartesian coordinates in the wavenumber domain and

$$E(\mathbf{k}, z) = \int_{\mathbb{R}^2} e(\mathbf{r}, z) e^{-j\mathbf{k}^T \mathbf{r}} d\mathbf{r}. \quad (12)$$

For any fixed $\mathbf{k} \in \mathbb{R}^2$, (11) is a second-order ordinary differential equation in z with constant coefficients whose general solution in the half-space $z \geq 0$ is of the form

$$E(\mathbf{k}, z) = E(\mathbf{k}) e^{j k_z(\mathbf{k}) z}, \quad (13)$$

where $E(\mathbf{k})$ is an arbitrary complex-valued coefficient and $k_z(\mathbf{k})$ is defined as

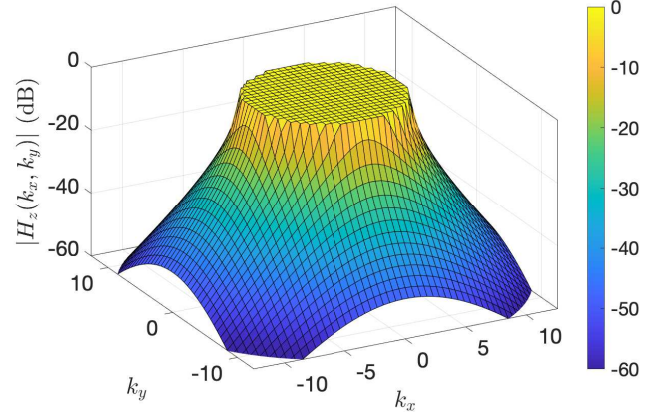
$$k_z(\mathbf{k}) = \sqrt{\kappa^2 - \|\mathbf{k}\|^2}. \quad (14)$$

Notice that \mathbf{k} can vary independently in \mathbb{R}^2 and hence $k_z(\mathbf{k})$ in (14) can be either real- or imaginary-valued with $\Im\{k_z(\mathbf{k})\} \geq 0$ according to (14).⁴ In particular, $k_z(\mathbf{k})$ is real-valued within the following wavenumber support:

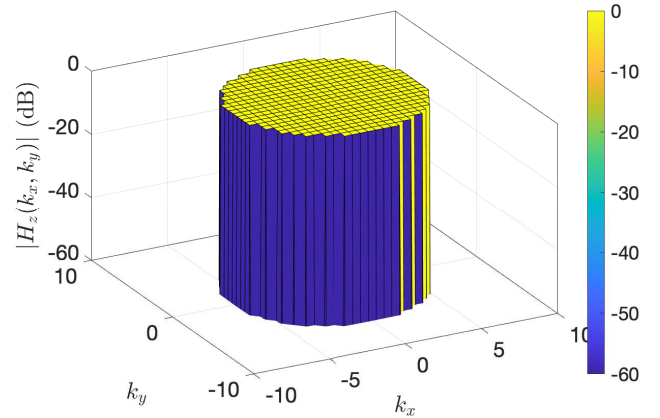
$$\mathcal{D} = \{\mathbf{k} \in \mathbb{R}^2 : \|\mathbf{k}\|^2 \leq \kappa^2\} \quad (15)$$

which is a centered disk of radius κ ; see Fig. 1. Outside this disk, $k_z(\mathbf{k})$ is imaginary-valued.

⁴Here, the positive sign is chosen to ensure that $e^{j k_z(\mathbf{k}) z}$ does not blow up at $z \rightarrow \infty$, which is known as the Sommerfeld's radiation condition [16].



(a) $z/\lambda = 1$.



(b) $z/\lambda = 10$.

Fig. 2. Magnitude of $H_z(\mathbf{k})$ in (17) (in dB) for different z .

The spatial field $e(\mathbf{r}, z)$ obeying (10) is obtained by taking the 2D inverse spatial Fourier transform of (13):

$$e(\mathbf{r}, z) = \frac{1}{(2\pi)^2} \int_{\mathbb{R}^2} E(\mathbf{k}) e^{j k_z(\mathbf{k}) z} e^{j\mathbf{k}^T \mathbf{r}} d\mathbf{k}, \quad z \geq 0. \quad (16)$$

B. An LSI Interpretation of Wave Propagation

A close inspection of (16) reveals that the spatial Fourier transform of $e(\mathbf{r}, z)$ is $E(\mathbf{k}) e^{j k_z(\mathbf{k}) z}$ and thus can be obtained by passing a 2D field $e(\mathbf{r}, 0)$ with arbitrary spectrum $E(\mathbf{k})$ through an LSI system (see Fig. 1) with wavenumber response

$$H_z(\mathbf{k}) = e^{j k_z(\mathbf{k}) z}, \quad z \geq 0. \quad (17)$$

This operation is known in physics as *migration* (e.g., [7, Sec. 7]), and it is a direct consequence of the Helmholtz equation in (10), which acts as an LSI operator projecting the number of observable 3D field configurations of $e(\mathbf{r}, z)$ onto a lower-dimensional 2D space [29]. Depending on \mathbf{k} , $H_z(\mathbf{k})$ in (17) is either an oscillatory or an exponentially-decaying function of z , i.e.,

$$H_z(\mathbf{k}) = \begin{cases} e^{j k_z(\mathbf{k}) z} & \mathbf{k} \in \mathcal{D} \\ e^{-|k_z(\mathbf{k})| z} & \mathbf{k} \notin \mathcal{D}. \end{cases} \quad (18)$$

In the case $\mathbf{k} \in \mathcal{D}$, $H_z(\mathbf{k})$ is an all-pass filter that simply introduces a phase-shift along z . This implies that $e(\mathbf{r}, z)$, at any z -plane with $z \geq z_0$ is fully determined by $e(\mathbf{r}, z_0)$. On the contrary, all wavevectors $\mathbf{k} \notin \mathcal{D}$ are attenuated at an exponential pace along z .

Notice that the support of $H_z(\mathbf{k})$ is not fixed but depends on z . This is quantified in Fig. 2 where the magnitude of $H_z(\mathbf{k})$ is plotted (in dB) for $z/\lambda = \{1, 10\}$. At $z = 10\lambda$, the field outside of \mathcal{D} is attenuated more than 60 dB. This means that, for distances z larger than a few wavelengths, we may consider $H_z(\mathbf{k})$ as a *circularly-bandlimited, low-pass filter* with fixed bandwidth

$$m(\mathcal{D}) = \pi\kappa^2 \quad (19)$$

which is the Lebesgue measure of (15). Notice that the bandwidth increases proportionally with the squared value of the operating frequency. Consequently, $e(\mathbf{r}, z)$ is a circularly-bandlimited field for any practical distance from scatterers.

C. Physics-based Plane-wave Interpretation

The integral representation of $e(\mathbf{r}, z)$ in (16) has an intuitive physical interpretation in terms of incoming plane-waves arriving from different directions. Particularly, $e(\mathbf{r}, z)$ is obtained as an integral superposition of the complex exponentials $e^{j(\mathbf{k}^T \mathbf{r} + k_z(\mathbf{k})z)}$ with the triplet $(\mathbf{k}, k_z(\mathbf{k}))$ such that $\|\mathbf{k}\|^2 + k_z^2(\mathbf{k}) = \kappa^2$. Hence, each complex exponential physically corresponds to a *plane-wave* impinging on the point (\mathbf{r}, z) from a propagation direction $(\mathbf{k}/\kappa, k_z(\mathbf{k})/\kappa)$ and having complex-valued amplitude $E(\mathbf{k})$, which is determined by the angular selectivity of the scattering mechanism [23]. There are two types of plane-waves in nature: *evanescent* and *propagating*. The former are associated to $\mathbf{k} \notin \mathcal{D}$, as their contribution to the field vanishes along z at an exponential rate, while the latter are associated to $\mathbf{k} \in \mathcal{D}$. In practice, only the propagating plane-waves contribute to the field $e(\mathbf{r}, z)$ and (16) can be thus approximated as:

$$e(\mathbf{r}, z) = \int_{\mathcal{D}} E(\mathbf{k}) e^{j(\mathbf{k}^T \mathbf{r} + k_z(\mathbf{k})z)} d\mathbf{k}. \quad (20)$$

An equivalent representation of (20) can be obtained in the angular domain via cosine directions, which can be conveniently related to spherical coordinates, i.e., elevation $\theta \in [0, \pi/2]$ and azimuth $\phi \in [0, 2\pi)$ angles (see, e.g., [23, App. D]). This yields

$$\begin{pmatrix} \mathbf{k} \\ k_z(\mathbf{k}) \end{pmatrix} = \begin{pmatrix} \kappa \sin(\theta) \cos(\phi) \\ \kappa \sin(\theta) \sin(\phi) \\ \kappa \cos(\theta) \end{pmatrix}. \quad (21)$$

Being interested in leveraging the correspondence with time-domain signals and Fourier theory, we do our analysis in the wavenumber domain. The angular domain representation will be used in Section VI to characterize the angular selectivity of the scattering.

IV. NYQUIST SAMPLING AND RECONSTRUCTION OF ELECTROMAGNETIC FIELDS

Consider an electromagnetic field $e(\mathbf{r}, z)$ with $\mathbf{r} = (x, y) \in \mathbb{R}^2$ that is observed over an infinite plane oriented parallel to

the arbitrarily chosen z -axis. We drop the functional dependence from z , i.e., $e(\mathbf{r}, z) = e(\mathbf{r})$, as the sole effect of wave propagation along the z -axis is to limit the spectral support of the field to $\mathbf{k} \in \mathcal{D}$ via migration. In this section, we first review the sampling theorem for a 2D field and apply it to solve the Nyquist sampling and reconstruction problems for a 3D electromagnetic field under different scattering conditions. We consider wave propagation into a deterministic environment whose configuration of the scatterers is known a priori. A statistical representation is treated in Section VI. We assume that the spectrum $E(\mathbf{k})$ of $e(\mathbf{r})$ is of general support $\mathcal{K} \subseteq \mathcal{D}$ that is centered around the origin of the wavenumber Cartesian axes. Physically, this corresponds to having the observation plane oriented towards the propagation direction specified by the centroid of the field's spectrum.

A. 2D Sampling

The generalization of the time-domain sampling (2) to a 2D lattice $\mathbf{r} = \mathbf{Q}\mathbf{n}$ with $\mathbf{n} = (n_x, n_y) \in \mathbb{Z}^2$ yields [6, Sec. 6]

$$e_s(\mathbf{r}) = \sum_{\mathbf{n} \in \mathbb{Z}^2} e(\mathbf{Q}\mathbf{n}) \delta(\mathbf{r} - \mathbf{Q}\mathbf{n}) \quad (22)$$

where $\mathbf{Q} \in \mathbb{R}^{2 \times 2}$ is a non-singular transformation matrix, called sampling matrix. As an example, a simple 2D rectangular sampling is obtained when $\mathbf{Q} = \text{diag}(q_x, q_y)$ where q_x and q_y are the sampling intervals along the x - and y -axis, respectively. The Fourier transform of $e_s(\mathbf{r})$ is [6, Sec. 6]

$$E_s(\mathbf{k}) = \sum_{\mathbf{n} \in \mathbb{Z}^2} e(\mathbf{Q}\mathbf{n}) e^{-j\mathbf{k}^T(\mathbf{Q}\mathbf{n})} \quad (23)$$

$$= \frac{1}{|\det(\mathbf{Q})|} \sum_{\boldsymbol{\ell} \in \mathbb{Z}^2} E(\mathbf{k} - \mathbf{P}\boldsymbol{\ell}) \quad (24)$$

where the periodicity matrix $\mathbf{P} \in \mathbb{R}^{2 \times 2}$ and the sampling matrix \mathbf{Q} are such that

$$\mathbf{P}^T \mathbf{Q} = 2\pi \mathbf{I}_2. \quad (25)$$

Perfect reconstruction of the field is possible if the periodicity matrix \mathbf{P} ensures no overlapping among adjacent wavenumber replicas of $E(\mathbf{k})$. The Nyquist periodicity matrix \mathbf{P}^* is the one that ensures minimum interspacing among adjacent spectra. The corresponding Nyquist sampling matrix is

$$\mathbf{Q}^* = 2\pi((\mathbf{P}^*)^T)^{-1} \quad (26)$$

as obtained from (25) and utilizes the minimum number of samples per unit of space, given by (in samples/m²) [7], [30]

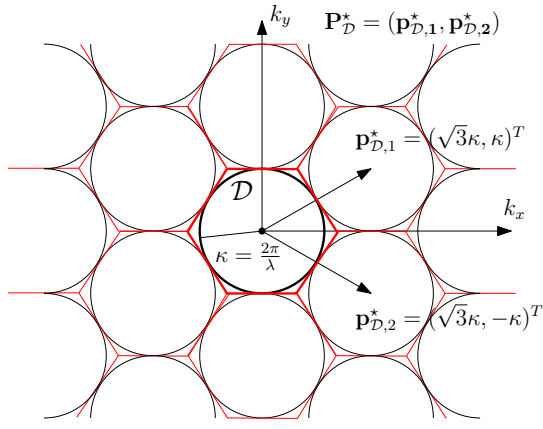
$$\mu = \frac{1}{|\det(\mathbf{Q}^*)|}. \quad (27)$$

As in (7), under Nyquist sampling, $E(\mathbf{k})$ can be perfectly retrieved by low-pass filtering $E_s(\mathbf{k})$, i.e.,

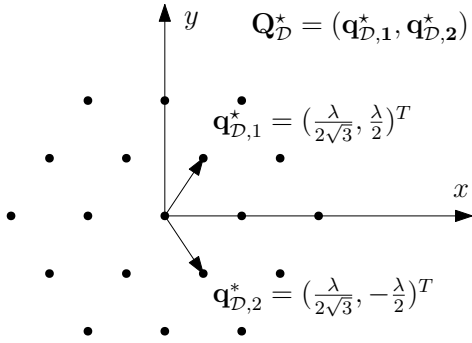
$$E(\mathbf{k}) = E_s(\mathbf{k}) (|\det(\mathbf{Q}^*)| \mathbb{1}_{\mathcal{K}}(\mathbf{k})). \quad (28)$$

The 2D cardinal series is obtained by taking the inverse Fourier transform of (28) with $E_s(\mathbf{k})$ in (23) that yields [6, Eq. (6.33)]:

$$e(\mathbf{r}) = \sum_{\mathbf{n} \in \mathbb{Z}^2} e(\mathbf{Q}^* \mathbf{n}) f_{\mathcal{K}}(\mathbf{r} - \mathbf{Q}^* \mathbf{n}) \quad (29)$$



(a) Circle packing in the wavenumber domain.



(b) Hexagonal sampling in the spatial domain.

Fig. 3. Nyquist sampling under isotropic scattering conditions.

with interpolating function [6, Eq. (6.34)]

$$f_{\mathcal{K}}(\mathbf{r}) = \frac{|\det(\mathbf{Q}^*)|}{(2\pi)^2} \int_{\mathbb{R}^2} \mathbb{1}_{\mathcal{K}}(\mathbf{k}) e^{i\mathbf{k}^T \mathbf{r}} d\mathbf{k}. \quad (30)$$

Notice that the Nyquist sampling matrix and interpolating function do not depend on the spectral characteristics of $E(\mathbf{k})$, but solely by the shape of its support \mathcal{K} . This is different from the time-domain case, where the Nyquist sampling and interpolating sinc-function are univocally determined by the bandwidth, i.e., the Lebesgue measure, of its frequency support. This is because a field may extend differently along its dimensions [8].

B. Isotropic Scattering

Suppose that $e(\mathbf{r})$ that has a spectrum $E(\mathbf{k})$ that is non-zero over $\mathbf{k} \in \mathcal{D}$, i.e., $e(\mathbf{r}) \in \mathcal{B}_{\mathcal{D}}$. This physically corresponds to an isotropic scattering condition where plane-waves carry equal power from all possible directions $\theta \in [0, \pi/2]$ and $\phi \in [0, 2\pi)$ [23], [24].

The problem of finding the Nyquist periodicity matrix $\mathbf{P}_{\mathcal{D}}^*$ is geometrically formulated as the arrangement of circles of equal radius κ on a 2D plane that achieves the highest density, i.e. a circle packing problem [7, Sec. 1.4], as illustrated in Fig. 3a. The solution is obtained by first inscribing each one of these circles with a regular hexagon of side lengths $2\kappa/\sqrt{3}$

(red line) and, then, replicating this hexagonal arrangement periodically such that no aliasing occurs [7, Eq. (1.148)]

$$\mathbf{P}_{\mathcal{D}}^* = \begin{pmatrix} \sqrt{3}\kappa & \sqrt{3}\kappa \\ \kappa & -\kappa \end{pmatrix}. \quad (31)$$

The Nyquist sampling matrix is obtained from (26) as in [7, Eq. (1.153)] while substituting $\kappa = 2\pi/\lambda$:

$$\mathbf{Q}_{\mathcal{D}}^* = \begin{pmatrix} \frac{\pi}{\kappa\sqrt{3}} & \frac{\pi}{\kappa\sqrt{3}} \\ \frac{\pi}{\kappa} & -\frac{\pi}{\kappa} \end{pmatrix} = \begin{pmatrix} \frac{\lambda}{2\sqrt{3}} & \frac{\lambda}{2\sqrt{3}} \\ \frac{\lambda}{2} & -\frac{\lambda}{2} \end{pmatrix} \quad (32)$$

and it corresponds to a *hexagonal sampling*, as illustrated in Fig. 3b. For the Nyquist sampling matrix $\mathbf{Q}_{\mathcal{D}}^*$ in (32), the Nyquist rate is computed from (27) as

$$\mu_{\mathcal{D}} = \frac{1}{|\det(\mathbf{Q}_{\mathcal{D}}^*)|} = \frac{2\sqrt{3}}{\lambda^2}. \quad (33)$$

Notice that $\mathbf{Q}_{\mathcal{D}}^*$ is not unique as there exist other sampling matrices all achieving the same Nyquist rate [8], [9], e.g., by rotating the wavenumber axes by $\pi/2$.

The interpolating function is generally obtained by computing the inverse spatial Fourier transform in (30) over the same wavenumber support that is used for determining the Nyquist sampling matrix. For any $e(\mathbf{r}) \in \mathcal{B}_{\mathcal{D}}$, this corresponds to the regular hexagon inscribing \mathcal{D} (see Fig. 3a). A suboptimal, yet accurate, interpolating function is obtained below by computing (30) over \mathcal{D} [8, Sec. VIII].

Lemma 1. Suppose that $e(\mathbf{r}) \in \mathcal{B}_{\mathcal{K}}$ with $\mathcal{K} = \mathcal{D}$, then perfect reconstruction of $e(\mathbf{r})$ can be achieved by using (29) with

$$f_{\mathcal{D}}(\mathbf{r}) = \frac{\pi}{\sqrt{3}} \text{jinc} \left(\frac{2\pi\|\mathbf{r}\|}{\lambda} \right). \quad (34)$$

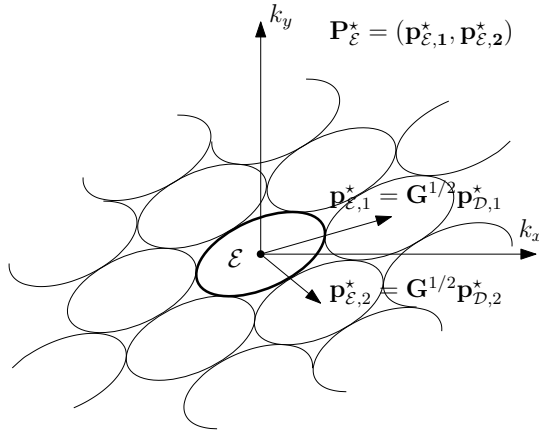
Proof. Despite this result is given already in [8, Eq. (74)], the proof is only sketched for a general multi-dimensional isotropically bandlimited field with multivariate argument $\mathbf{r} \in \mathbb{R}^N$. Since this result is preparatory for the non-isotropic scattering, the proof is given in Appendix A. \square

The above interpolating function provides a high reconstruction accuracy while limiting the complexity due to its rotational symmetry. This can also be easily extended to non-isotropic scenarios, as studied next.

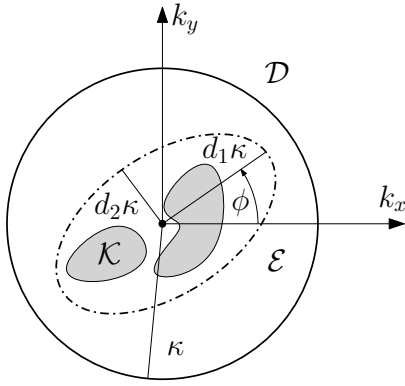
C. Non-isotropic Scattering

Wave propagation in its most general form is non-isotropic. This amounts to assuming that the spectrum $E(\mathbf{k})$ has support $\mathcal{K} \subseteq \mathcal{D}$, i.e., $e(\mathbf{r}) \in \mathcal{B}_{\mathcal{K}}$, as shown in Fig. 1 [23], [24]. Clearly, $\mathcal{K} = \mathcal{D}$ under isotropic scattering conditions. Finding the Nyquist periodicity matrix $\mathbf{P}_{\mathcal{K}}^*$ in non-isotropic conditions is generally too complicated: (i) \mathcal{K} should be an analytically describable region (e.g., a circle or a rectangle); (ii) for a non-connected spectrum one would have to find the tightest embedding (with minimum Lebesgue measure) of \mathcal{K} ; and (iii) we should be able to solve the resulting \mathcal{K} -packing problem geometrically [8].

In general, due to the above difficulties in solving the optimal Nyquist sampling problem, we resort to a sub-optimal



(a) Ellipse packing in the wavenumber domain.



(b) Affine mapping between circle and ellipse.

Fig. 4. Nyquist sampling under non-isotropic scattering conditions.

solution through the embedding of \mathcal{K} into a larger and connected support. A possible embedding of \mathcal{K} is into a 2D ellipse $\mathcal{E} \subseteq \mathcal{K}$ as illustrated in Fig. 4b. This is defined as [31, Sec. 2]

$$\mathcal{E} = \{\mathbf{k} \in \mathbb{R}^2 : \mathbf{k}^T \mathbf{G}^{-1} \mathbf{k} \leq \kappa^2\} \quad (35)$$

where $\mathbf{G} \in \mathbb{R}^{2 \times 2}$ is a symmetric and positive definite matrix (i.e., nonsingular) that specifies how the ellipse extends in every direction from its center, called transformation matrix. Clearly, \mathcal{D} in (15) is obtained as a particular instance of (35) by setting $\mathbf{G} = \mathbf{I}_2$. Although other embeddings may be used (e.g., square, circle, and rectangle), the elliptical embedding is tight and analytically tractable. The Nyquist sampling matrix is as follows.

Lemma 2. Suppose that $e(\mathbf{r}) \in \mathcal{B}_{\mathcal{K}}$ with $\mathcal{K} \subseteq \mathcal{E}$, then the Nyquist sampling matrix $\mathbf{Q}_{\mathcal{E}}^*$ is given by

$$\mathbf{Q}_{\mathcal{E}}^* = (\mathbf{G}^{-1/2})^T \mathbf{Q}_{\mathcal{D}}^* \quad (36)$$

where $\mathbf{Q}_{\mathcal{D}}^*$ is defined in (32) and \mathbf{G} is the transformation matrix in (35).

Proof. The proof is given in Appendix B and is built upon the affine mapping $\varphi : \mathcal{D} \rightarrow \mathcal{E}$ that turns circles into ellipses. \square

Notice that $\mathbf{Q}_{\mathcal{E}}^*$ in Lemma 2 is obtained as a product between the isotropic Nyquist sampling matrix $\mathbf{Q}_{\mathcal{D}}^*$ and the inverse transformation matrix $(\mathbf{G}^{-1/2})^T$. Consequently, the Nyquist sampling in this case is a rotated and scaled version of the one obtained under isotropic scattering conditions, i.e., an *elongated hexagonal sampling*. How the hexagonal sampling is stretched in space is determined by the transformation matrix \mathbf{G} in (69), whose parameters are uniquely determined by the configuration of the scatterers.

For the Nyquist sampling matrix $\mathbf{Q}_{\mathcal{E}}^*$ in (36), the Nyquist rate is computed from (27) as

$$\mu_{\mathcal{E}} = \frac{1}{|\det(\mathbf{Q}_{\mathcal{E}}^*)|} \stackrel{(a)}{=} \frac{\sqrt{d_1 d_2}}{|\det(\mathbf{Q}_{\mathcal{D}}^*)|} \stackrel{(b)}{=} \sqrt{d_1 d_2} \mu_{\mathcal{D}} \quad (37)$$

where (a) follows from (36) and the unitary property of rotation matrices, and (b) from (33). Here, d_1 and d_2 are the (normalized) lengths of the semi-axes of \mathcal{E} in (35) (see Fig. 4b). Since $0 \leq d_1, d_2 \leq 1$, we have that $\mu_{\mathcal{E}} \leq \mu_{\mathcal{D}}$ from which we see that the elongated hexagonal sampling yields the following *sampling efficiency gain* equal to

$$1 - \frac{\mu_{\mathcal{E}}}{\mu_{\mathcal{D}}} = 1 - \sqrt{d_1 d_2} \quad (38)$$

As an example, consider the case where we receive power from the entire azimuthal horizon but half range in elevation angle. This is modeled as a centered ellipse \mathcal{E} of parameters $d_1 = 1$ and $d_2 = 0.5$. The sampling efficiency gain in (38) is approximately 30%. Notice that this gain is insensitive to an arbitrary rotation of the spectrum, as (38) is not a function of the rotation angle ϕ .

The interpolating function for the elliptical embedding is given next.

Lemma 3. Suppose that $e(\mathbf{r}) \in \mathcal{B}_{\mathcal{K}}$ with $\mathcal{K} \subseteq \mathcal{E}$, then perfect reconstruction of $e(\mathbf{r})$ can be achieved by using (29) with

$$f_{\mathcal{E}}(\mathbf{r}) = \frac{\pi}{\sqrt{3}} \text{jinc} \left(\frac{2\pi \|\mathbf{D}^{1/2} \mathbf{r}\|}{\lambda} \right) \quad (39)$$

where $\mathbf{D} = \text{diag}(d_1, d_2) \in \mathbb{R}^{2 \times 2}$ is diagonal with elements given by the (normalized) lengths of the semi-axes of \mathcal{E} in (35).

Proof. The proof is given in Appendix C. \square

Notice that (39) is obtained from its isotropic counterpart (34) by applying the same affine map used for sampling, except for the rotation, as it has no effect on $f_{\mathcal{D}}(\mathbf{r})$.

D. Half-wavelength Rectangular Sampling

The classical half-wavelength rectangular sampling arises as the Nyquist sampling for a spectrum with wavenumber support

$$\mathcal{R} = \{\mathbf{k} = (k_x, k_y) \in \mathbb{R}^2 : |k_x| \leq \kappa, |k_y| \leq \kappa\} \quad (40)$$

which corresponds to the rectangle circumscribing the disk \mathcal{D} . Based on the physical interpretation given in Section III-C, this implies that a portion of the evanescent waves spectrum contributes to the generation of the field, which happens only when the observation plane is located in the close proximity of the scatterers (see Fig. 2). The Nyquist periodicity matrix $\mathbf{P}_{\mathcal{R}}^*$ is geometrically found by solving a 2D square packing

problem of equal side length 2κ . Due to the rectangular symmetry of \mathcal{R} in (40), this is solved as a (one-dimensional) 1D problem, e.g., along the k_x -axis. The Nyquist sampling interval follows from (6) as $Q_x^* = \pi/\kappa = \lambda/2$ while using $\kappa = 2\pi/\lambda$. Exchanging the k_x - and k_y -axes and rearranging the results into a matrix form yields

$$\mathbf{Q}_{\mathcal{R}}^* = \frac{\lambda}{2} \mathbf{I}_2. \quad (41)$$

The Nyquist rate corresponding to (41) is given by

$$\mu_{\mathcal{R}} = \frac{1}{|\det(\mathbf{Q}_{\mathcal{R}}^*)|} = \frac{4}{\lambda^2} \quad (42)$$

which, compared to (33), reveals that a hexagonal sampling is

$$1 - \frac{\mu_{\mathcal{D}}}{\mu_{\mathcal{R}}} = 1 - \frac{\sqrt{3}}{2} = 13.4\% \quad (43)$$

more efficient than rectangular sampling [7, Sec. 1.4]. Hence, a rectangular sampling should be used in wireless applications operating in the reactive near-field region only, as some of the samples are linearly redundant each other.

The interpolating function for the reconstruction of $e(\mathbf{r}) \in \mathcal{B}_{\mathcal{R}}$ follows analogously to the time-domain case by separability of (40). Particularly, this is obtained from $f_{\Omega}(t) = \text{sinc}(\Omega t/\pi)$ while replacing Ω with the wavenumber bandwidth $\kappa = 2\pi/\lambda$ and replicating over the y -axis as

$$f_{\mathcal{R}}(\mathbf{r}) = \text{sinc}\left(\frac{2x}{\lambda}\right) \text{sinc}\left(\frac{2y}{\lambda}\right). \quad (44)$$

E. 3D Reconstruction

As seen in Section III, the propagation behaviour of $e(\mathbf{r})$ along z is exactly known a-priori. In particular, for values of z larger than few wavelengths, the electromagnetic field measured at any z plane is nonetheless a space-shifted version of itself. Thus, once the 2D field $e(\mathbf{r}, z_0)$ with $z_0 \geq 0$ is reconstructed through (29), the 3D volumetric reconstruction of $e(\mathbf{r}, z)$ for any $z \geq z_0$ is simply achieved via a constant phase-shift. Differently from classical 3D volumetric reconstruction of an object, electromagnetic fields require to capture a single (not multiple) ‘‘image’’ of the field.

V. DEGREES OF FREEDOM OF ELECTROMAGNETIC FIELDS

The DoF of a time-domain signal $e(t) \in \mathcal{B}_{\Omega}$ that can be extracted from an interval of duration T are directly obtained by the cardinal series in (1), due to orthogonality of the shifted-versions of $f_{\Omega}(t)$ as $\Omega T \rightarrow \infty$ [5, Eq. (5)]. The Shannon’s approach extends to $e(\mathbf{r}) \in \mathcal{B}_{\mathcal{R}}$, defined over a 2D squared region $\mathcal{A} \subseteq \mathbb{R}^2$ of side length L , because of the separability and orthogonal properties of $f_{\mathcal{R}}(\mathbf{r})$ in (44) as $L/\lambda \rightarrow \infty$. Within a segment of length L , since there are $2/\lambda$ samples/m, the number of significant samples in the region \mathcal{A} is

$$\text{dof}_{\mathcal{R}} = \left[\left(\frac{2L}{\lambda} \right)^2 \right] = \left[\left(\frac{\kappa L}{\pi} \right)^2 \right] \quad (45)$$

which is the 2D spatial counterpart to the Shannon’s DoF formula (8). The physical implication of (45) is that only a finite number of propagation directions carries the information

contained in the field and can be used to reconstruct it. The reconstruction error becomes negligible as $L/\lambda \rightarrow \infty$. By rewriting (45) in terms of the field’s bandwidth $m(\mathcal{R}) = 4\kappa^2$ and observation area $m(\mathcal{A}) = L^2$ yields

$$\text{dof}_{\mathcal{R}} = \left[\frac{m(\mathcal{A})m(\mathcal{R})}{(2\pi)^2} \right] \quad (46)$$

which coincides to the Landau’s DoF formula [29], [32].

Solving the Nyquist sampling problem exactly for any \mathcal{K} of arbitrary shape is hard without recurring to an embedding, which is true even under isotropic propagation; see Fig. 3a. Consequently, the shifted-versions of $f_{\mathcal{K}}(\mathbf{r})$ in (29) are not orthogonal in general. A possible orthogonal basis set of functions over $\mathbf{r} \in \mathcal{A}$ is represented by the 2D Fourier harmonics with fundamental frequency of $2\pi/L$ rad/m. This yields the Fourier series expansion, which provides an exact representation of $e(\mathbf{r})$ asymptotically as $L/\lambda \rightarrow \infty$. Under isotropic scattering, i.e., $\mathbf{k} \in \mathcal{D}$, since the wavenumber samples are taken at $2\pi/L$ rad/m apart, we have that [1, Eq. (18)]

$$\text{dof}_{\mathcal{D}} = \left[\pi \left(\frac{L}{\lambda} \right)^2 \right] = \left[\frac{m(\mathcal{A})m(\mathcal{D})}{(2\pi)^2} \right] \quad (47)$$

where we have used $m(\mathcal{D}) = \pi\kappa^2$. Particularly, (47) is obtained by rescaling the wavenumber Cartesian axes by $L/2\pi$ and solving the Gauss circle problem [33]. Notice that

$$1 - \frac{\text{dof}_{\mathcal{R}}}{\text{dof}_{\mathcal{D}}} = 1 - \frac{m(\mathcal{D})}{m(\mathcal{R})} = 1 - \frac{\pi}{4} \approx 21.5\% \quad (48)$$

from which it follows that roughly one-fifth of the DoF generated by the wave propagation mechanism are confined in a region of a few wavelengths surrounding the scatterers. Building on the above results, the number of DoF under non isotropic scattering is obtained

$$\text{dof}_{\mathcal{K}} = \left[\frac{m(\mathcal{A})m(\mathcal{K})}{(2\pi)^2} \right]. \quad (49)$$

With an elliptical embedding, (49) reduces to

$$\text{dof}_{\mathcal{E}} = \left[\frac{m(\mathcal{A})m(\mathcal{E})}{(2\pi)^2} \right] \stackrel{(a)}{=} \sqrt{d_1 d_2} \left[\frac{m(\mathcal{A})m(\mathcal{D})}{(2\pi)^2} \right] \quad (50)$$

$$= \sqrt{d_1 d_2} \text{dof}_{\mathcal{D}} \quad (51)$$

where (a) follows from the affine mapping $\varphi : \mathcal{D} \rightarrow \mathcal{E}$, which yields the following relation in terms of Lebesgue measure:

$$m(\mathcal{E}) = m(\mathcal{D}) |\det(\mathbf{G}^{1/2})| = m(\mathcal{D}) \sqrt{d_1 d_2}. \quad (52)$$

Since $0 \leq d_1, d_2 \leq 1$, it thus follows that $\text{dof}_{\mathcal{E}} \leq \text{dof}_{\mathcal{D}}$, as it should be (see, e.g., [19]). In fact, non-isotropic scattering implies a reduced dimensionality of the function space spanned by the field, which translates into a lower number of DoF. This is the reason why a lower Nyquist sampling rate is required with non-isotropic scattering; see (37) and (38).

When \mathcal{A} is a 1D segment of length L , by restricting the wavenumber domain to one of the two Cartesian axes, e.g., the x -axis, we have that $k_x \in [-\kappa, \kappa]$. Hence, the DoF are computed similarly to the time-domain case by using the time-frequency and space-wavenumber duality [1, Sec. III]. These are given by $2L/\lambda$. The expansion of a 2D rectangle into

a 3D volume does not create any additional DoF [1], [25]. This is a direct consequence of the migration filter, which linearly relates the field's configurations at different z -planes and have its roots in the Huygen's electromagnetic principle [20, Sec. III.F] [34].

VI. SPATIALLY-STATIONARY RANDOM ELECTROMAGNETIC FIELDS

So far, we have considered a deterministic representation of the electromagnetic field that is a priori known. However, this assumption requires an accurate predictions of wave propagation, which relies on numerical electromagnetic solvers of the Maxwell's equations, and hence, it is too site-specific [11]. The common way out to (statistically) embrace different propagation conditions is by modeling the field as a multidimensional random process (or random field) of electromagnetic nature. Particularly, we model $e(\mathbf{r})$ as a zero-mean, circularly-symmetric, complex-Gaussian, and stationary spatial random field [23]–[26].

A. Spectral Characterization

For a spatially-stationary $e(\mathbf{r})$ with $\mathbf{r} \in \mathbb{R}^2$ its autocorrelation function $c(\mathbf{r}) = \mathbb{E}\{e(\mathbf{r}')e^*(\mathbf{r}' + \mathbf{r})\}$ obeys the Helmholtz equation in (10) [25, Eq. (4)]:

$$\nabla^2 c(\mathbf{r}) + \kappa^2 c(\mathbf{r}) = 0. \quad (53)$$

An analogue procedure developed in Section III for a deterministic $e(\mathbf{r})$ yields [24], [25]:

$$c(\mathbf{r}) = \frac{1}{(2\pi)^2} \int_{\mathbb{R}^2} S(\mathbf{k}) e^{j\mathbf{k}^T \mathbf{r}} d\mathbf{k} \quad (54)$$

where the 2D power spectral density of $e(\mathbf{r})$ is defined as

$$S(\mathbf{k}) = \frac{A^2(\mathbf{k})}{k_z(\mathbf{k})}, \quad \mathbf{k} \in \mathcal{D} \quad (55)$$

with $A(\mathbf{k})$ being an arbitrary real-valued non-negative function, called *spectral factor*. Compared to (16), the integration region is restricted to $\mathbf{k} \in \mathcal{D}$ as $k_z(\mathbf{k})$ must be real-valued in order for $c(\mathbf{r})$ to satisfy the standard Hermitian-symmetry property for any $\mathbf{r} \in \mathbb{R}^2$.

The random field $e(\mathbf{r})$ is obtained by expanding a circularly-symmetric complex white-noise field $W(\mathbf{k})$ with unit variance over the same 2D Fourier basis in (54), which is in the form of a 2D *Fourier spectral representation* of $e(\mathbf{r})$ [24, Sec. III.C]:

$$e(\mathbf{r}) = \frac{1}{2\pi} \int_{\mathbb{R}^2} S^{1/2}(\mathbf{k}) W(\mathbf{k}) e^{j\mathbf{k}^T \mathbf{r}} d\mathbf{k}. \quad (56)$$

The convergence of (56) to the actual random field holds in the mean-squared sense, for any bounded spectral factor [24].

We can interpret $e(\mathbf{r})$ in (56) as physically generated by the superposition of a continuum of *propagating* plane-waves, each one of which has circularly-symmetric complex-Gaussian amplitude $E(\mathbf{k}) = S^{1/2}(\mathbf{k})W(\mathbf{k})$ that is statistically independent from one direction to another [24], [25].

B. DoF and Reconstruction

The computation of the DoF of a stationary random process requires to identify a basis set of functions that yields uncorrelated coefficients – also statistically independent for a jointly Gaussian process. This is at the basis of the Karhunen-Loeve series expansion [35, Sec. 3.3.2]. Finding this basis set is hard in practice, as an explicit solution is only available for a few cases. As an example, for a stationary random process $e(t)$ with a constant and bandlimited spectrum, it can be found by solving the Slepian's concentration problem [32] [27, Sec. 2]. The same theory extends to a multiple dimension stationary random field $e(\mathbf{r})$ of constant and bandlimited spectrum [29], [27, Sec. 3].

A way to overcome the difficulty in finding a Karhunen-Loeve series expansion of a random field is to operate in the *asymptotic regime*. Particularly, in the time domain, as the observation interval T of $e(t)$ becomes large, i.e., $\Omega T \gg 1$, the Karhunen-Loeve series expansion becomes a Fourier series expansion with statistically independent Fourier coefficients [35, Sec. 3.4.6]. The same is true in the spatial domain as $L\kappa \gg 1$ (or $L/\lambda \gg 1$) due to the time-frequency and space-wavenumber duality [24, Sec. V]. Given this, the results derived in Section IV and Section V for a deterministic field can be extended to every ensemble of a random electromagnetic field $e(\mathbf{r})$ after replacing the field's spectrum with its power spectral density and must be interpreted on average.

The reconstruction of $e(\mathbf{r})$ from its Nyquist samples can be regarded as a statistical estimation problem [9]. Within a region of space $\mathcal{A} \subseteq \mathbb{R}^2$, the number N of observable samples is given by

$$N = m(\Lambda(\mathcal{A})) = \lceil \mu m(\mathcal{A}) \rceil \quad (57)$$

where μ is the Nyquist rate at which the samples are taken. One way to solve the above estimation problem is to use the 2D cardinal series in (29) while truncating the series expansion up to N terms:

$$\hat{e}(\mathbf{r}) = \sum_{\mathbf{n} \in \Lambda(\mathcal{A})} e(\mathbf{Q}^* \mathbf{n}) f_{\mathcal{K}}(\mathbf{r} - \mathbf{Q}^* \mathbf{n}) \quad (58)$$

where we denote with $\Lambda(\mathcal{A}) \subseteq \mathbb{Z}^2$ the truncated 2D lattice. Under the Nyquist condition, it turns out that (58) provides us with the best linear interpolator of $e(\mathbf{r})$ in the MSE sense, which is based on observed field's values $e(\mathbf{Q}^* \mathbf{n})$ with $\mathbf{n} \in \Lambda(\mathcal{A})$ [8, Sec. VI] [9, Sec. III]. Notice that the MSE vanishes as the area of the observation region increases.

VII. NUMERICAL ANALYSIS

Numerical results are provided next to validate the above results on Nyquist sampling and field's reconstruction in a non-asymptotic regime, i.e., finite L/λ values. Simulations are carried out for a stationary random electromagnetic field under isotropic and non-isotropic scattering conditions, which are analytically modelled next.

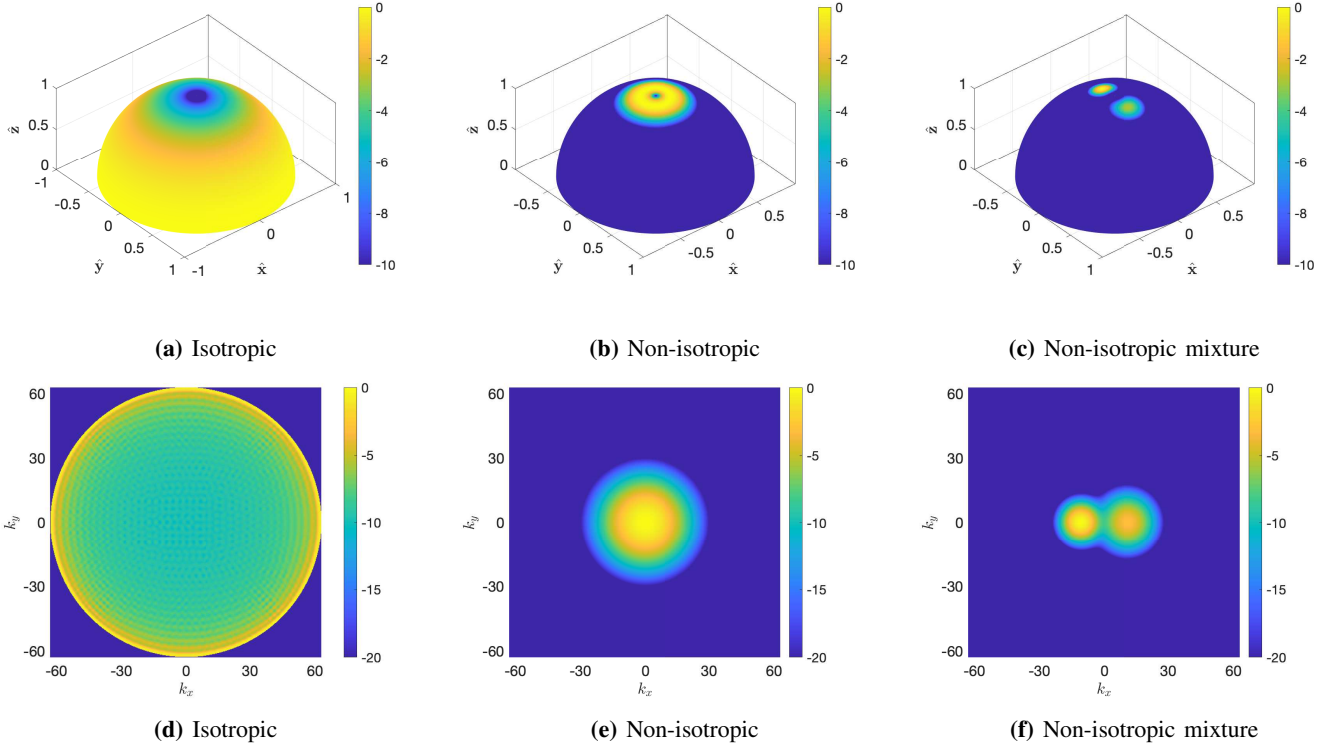


Fig. 5. Scattering under isotropic and non-isotropic conditions. The first row shows the spectral factor $\sin(\theta)A(\theta, \phi)$ in (62) with $(\theta, \phi) \in [0, \pi/2] \times [0, 2\pi)$. The second row shows the power spectral density $S(\mathbf{k})$ in (55) with $\mathbf{k} \in \mathcal{D}$.

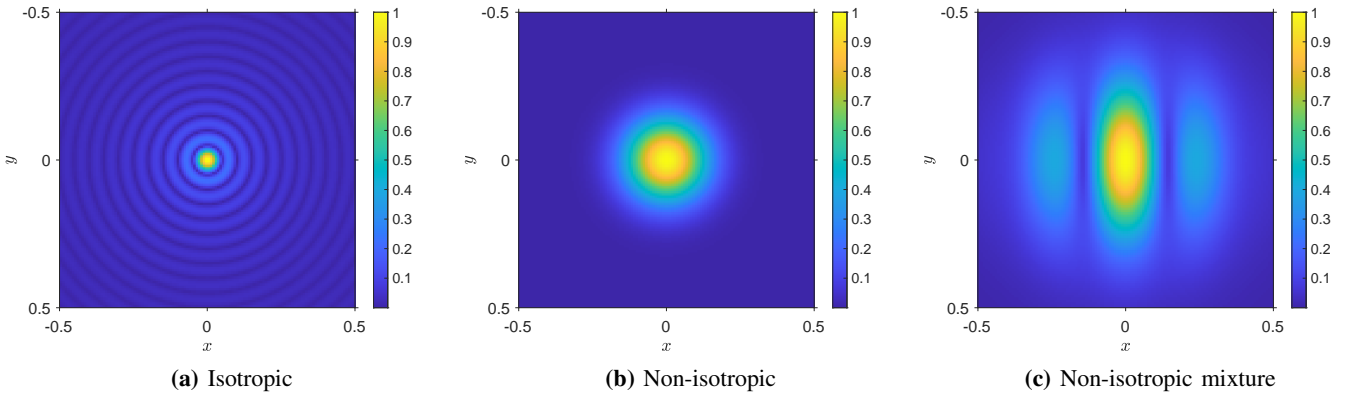


Fig. 6. Autocorrelation function $c(\mathbf{r})$ in (59) under the scattering conditions of Fig. 5.

A. Isotropic and Non-isotropic Conditions

In spherical coordinates, i.e., elevation $\theta \in [0, \pi/2]$ and azimuth $\phi \in [0, 2\pi)$ angles, (54) can be rewritten as

$$c(\mathbf{r}) \stackrel{(a)}{=} \int_0^{\pi/2} \int_0^{2\pi} A^2(\theta, \phi) e^{j\mathbf{k}^T(\theta, \phi)\mathbf{r}} \sin(\theta) d\theta d\phi \quad (59)$$

$$\stackrel{(b)}{=} \int_0^{\pi/2} \int_0^{2\pi} A^2(\theta, \phi) e^{j\kappa \sin(\theta)(\cos(\phi)x + \sin(\phi)y)} \sin(\theta) d\theta d\phi \quad (60)$$

where (a) follows from using the Jacobian $d\mathbf{k}/k_z(\mathbf{k}) \propto \sin(\theta)d\theta d\phi$ and (b) is obtained from (21) [23, App. D]. Here, constant terms due to change of integration variables are embedded into $A^2(\theta, \phi)$.

An isotropic scattering scenario can be modeled by setting $A(\theta, \phi) = 1$. The isotropic spectral factor $\sin(\theta)$ (inclusive of the Jacobian) is plotted in Fig. 5a on the upper hemisphere $(\theta, \phi) \in [0, \pi/2] \times [0, 2\pi)$. In the wavenumber domain, we have that $A(\mathbf{k}) = 1$ so that the power spectral density in (55) is given by $S(\mathbf{k}) = 1/k_z(\mathbf{k})$ for $\mathbf{k} \in \mathcal{D}$, as plotted in Fig. 5d. Here, $e(\mathbf{r})$ has a spectrum that is non-zero over $\mathbf{k} \in \mathcal{D}$, as we expected from the deterministic case in Fig. 1 and Fig. 3a. The isotropic autocorrelation function follows from (59) by setting $x = \|\mathbf{r}\|$ and $y = 0$ (due to polar symmetry) as

$$c(\mathbf{r}) = \text{sinc}(2\|\mathbf{r}\|/\lambda) \quad (61)$$

which coincides to the Clarke's autocorrelation function [36, Sec. 2.4]; see Fig. 6a. Non-isotropic scattering conditions can be considered alike by specifying a non-uniform spectral factor

$A(\theta, \phi)$. A general multi-clustered propagation environment can be modeled as a mixture of spectral factors [23, Sec. V]

$$A^2(\theta, \phi) = \sum_{i=1}^{N_c} w_i A_i^2(\theta, \phi) \quad (62)$$

weighted by $w_i \geq 0$ whose sums yields 1. Here, $A_i^2(\theta, \phi)$ is representative of the i -th cluster. One way to model $A_i^2(\theta, \phi)$ is by using the 3D von Mises-Fisher family of density distributions [23, Sec. V]. This is characterized by having circular level curves and it is specified by the lowest number of parameters, i.e., a modal direction

$$\hat{\xi}_i = \begin{pmatrix} \sin(\theta_{r,i}) \cos(\phi_{r,i}) \\ \sin(\theta_{r,i}) \sin(\phi_{r,i}) \\ \cos(\theta_{r,i}) \end{pmatrix} \quad (63)$$

which specifies the propagation direction (i.e., $(\theta_{r,i}, \phi_{r,i})$) around which the power is concentrated, and an angular concentration $\alpha_i \in [0, \infty)$ that describes the concentration level around $\hat{\xi}_i$ [23, Sec. V]. Notice that the isotropic scattering is obtained from (62) by setting $N_c = 1$ and $\alpha = 0$. Non-isotropic scattering is considered in Fig. 5b and Fig. 5c.

In Fig. 5b, we have a single cluster with $\theta_r = \phi_r = 0^\circ$, and α such that the normalized circular variance is $\nu^2 = 0.05$. The wavenumber domain is showed in Fig. 5e where we have a centered circular support \mathcal{K} of approximately 0.47κ radius, i.e., $d_1 = d_2 = 0.47$, which is measured by considering the bandwidth at -20 dB. We will see that this criterion provides a sufficiently accurate measure of the field's spectral support. The autocorrelation functions $c(\mathbf{r})$ is reported in Fig. 6b and shows an increased coherence area with respect to the isotropic case, due to angular selectivity of the scattering.

A two-clustered scenario with uniform weighting and parameters $(\theta_{r,1}, \phi_{r,1}) = [-10^\circ, 0^\circ]$, $(\theta_{r,2}, \phi_{r,2}) = [10^\circ, 0^\circ]$, and $\nu^2 = \{0.01, 0.02\}$ is shown in Fig. 5c and Fig. 5f in both representation domains. As seen, under non-isotropic scattering, \mathcal{K} may assume an arbitrary shape, as first assumed in the deterministic settings in Fig. 1 and Fig. 4b. This is embedded in Fig. 5f into an ellipse \mathcal{E} in (35) with $d_1 = 0.5$ and $d_2 = 0.35$. The autocorrelation functions for this non-isotropic case is given in Fig. 6c and shows the impact of asymmetries in the wavenumber spectrum on $c(\mathbf{r})$.

B. DoF and Nyquist Sampling

To quantify the impact of Nyquist sampling and the number of DoF, we consider the eigenvalues of the spatial correlation matrix $\mathbf{C} \in \mathbb{C}^{N \times N}$, obtained under the scattering conditions depicted in Fig. 5 and a squared region \mathcal{A} of side length $L = 10\lambda$ (i.e., $m(\mathcal{A}) = 100\lambda^2 \text{ m}^2$). In the isotropic scenario, \mathbf{C} is obtained by sampling (61) according to (32). For any non-isotropic scenario, we sample (59) by using (36). Comparisons are made with the half-wavelength rectangular sampling in (41). The number of DoF is computed on the basis of the results in Section V and is compared to the number of samples sufficient to capture 99.7% of the total field's power. This will be slightly higher because of the finite value of L/λ .

In Fig. 7a, the isotropic case is studied. From (47), we obtain $\text{dof}_{\mathcal{D}} = 315$ while 354 eigenvalues are obtained with

the 99.7% criterion. The number of DoF at 99.7% with $\lambda/2$ sampling increases up to 382. This is not due to the oversampling but to larger area; notice that it is numerically impossible to fit the hexagonal and rectangular grids within a given area.⁵ The number of observable samples of the $\lambda/2$ sampling is higher than the one of hexagonal sampling while providing the same (?) significant number of eigenvalues, and hence, it is less efficient.

The non-isotropic cases are considered in Fig. 7b and Fig. 7c. From (49), the number of DoF reduces to $\text{dof}_{\mathcal{K}} = 71$ and $\text{dof}_{\mathcal{K}} = 35$. This is due to the scattering mechanism that cuts off some of the resolvable propagation directions. Compared to Fig. 7a, the eigenvalue curves decay rapidly due to the spatial correlation; see also Fig. 6. The Nyquist sampling exhibits a slightly higher correlation than rectangular sampling, which is due to the numerical approximation of the field's spectral support with the -20 dB criterion.

From Fig. 7a, it follows that spatial correlation exists even under isotropic propagation (see also [11, Sec. IV]). This is because the autocorrelation function is not sampled at its zeros, as illustrated in Fig. 8. However, notice that the hexagonal sampling in the isotropic case is the one that exploits the available number of DoF per unit of area.

C. Reconstruction

A numerical example is provided in Fig. 9 to verify the reconstruction procedure under the scattering conditions of Fig. 5b. We sample $e(\mathbf{r})$ at Nyquist rate within a squared region of space \mathcal{A} of side length $L = 20\lambda$ and $L = 150\lambda$. The reconstruction formula in (58) is used to estimate the real part of $e(\mathbf{r})$ within a segment $x \in [-L/2, L/2]$ of length $L = 1$ m along the x -axis. The number N of samples used for reconstruction is obtainable from (57) by using the Nyquist rate in (37), i.e., $\mu_{\mathcal{E}} = 0.47\mu_{\mathcal{D}}$. At $\lambda = 0.1$ m, we have that $N = 9$. As seen in Fig. 9a, at $L = 10\lambda$, the reconstruction error is non-zero due to the truncation of the 2D cardinal series up to N terms. Nevertheless, this error is small as only a tiny contribution to the reconstruction is added by the tails of the interpolating function $f_{\mathcal{K}}(\mathbf{r})$. This effect vanishes as L/λ increases, as N also grows large as well. The error is negligible at $L = 150\lambda$, as shown in Fig. 9b.

VIII. CONCLUSIONS

We applied signal processing tools (e.g., multidimensional sampling theorem and Fourier theory) to study the Nyquist sampling and number of DoF of a scalar electromagnetic field, under arbitrary scattering conditions. We showed that 3D wave propagation can be modeled as a 2D circularly-bandlimited LSI low-pass filter that physically cuts off some of the propagating directions generated by the scatterers – those associated with evanescent waves, whose existence is confined to the reactive propagation region of the scatterers. The conventional half-wavelength rectangular sampling generally provides an oversampling of the field, as it coincides with the

⁵This effect is even more pronounced in the non isotropic scenario, due the sparsity of the elongated hexagonal sampling.

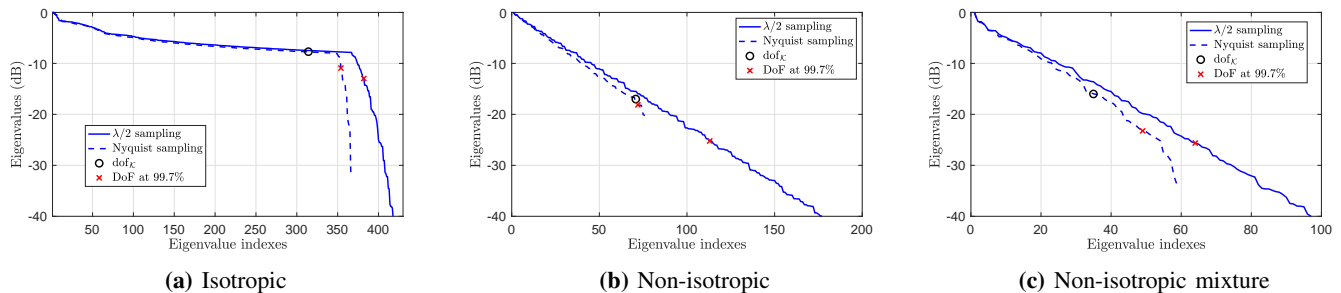


Fig. 7. Eigenvalues of \mathbf{C} reported in dB in a descending order under the scattering conditions depicted in Fig. 5. Samples of the random field are collected within a squared region \mathcal{A} of side length $L = 10\lambda$.

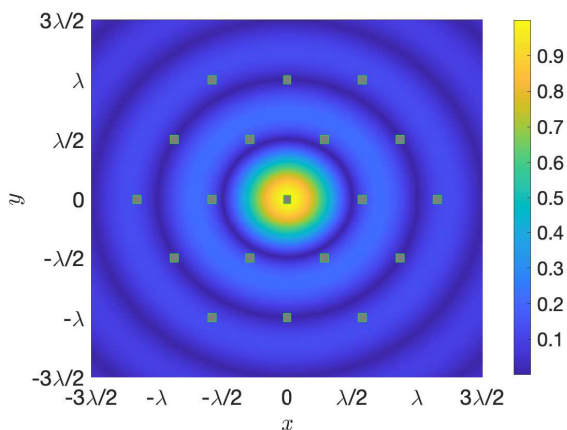


Fig. 8. The hexagonal sampling in Fig. 3b is plotted against the isotropic autocorrelation function $c(\mathbf{r})$ in (61).

Nyquist sampling only when the evanescent waves are taken into account. Other more efficient sampling structures, such as (elongated) hexagonal sampling, must be considered at a practical distance from scatterers (i.e., few wavelengths).

Sampling at Nyquist rate allows to fully capture the DoF offered by the electromagnetic field with the lowest number of samples. This feature may be crucial in communications at very high frequencies (e.g., in terahertz spectrum), where digital signal processing and hardware power consumption are both critical concerns.

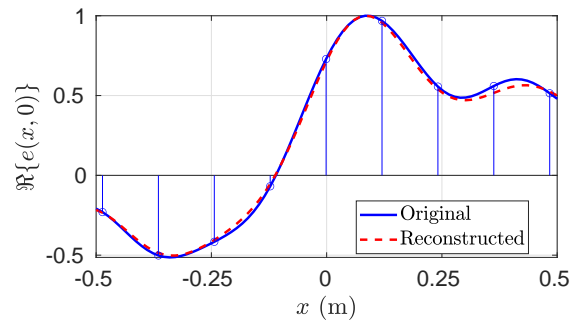
APPENDIX A

From (30), for a wavenumber support $\mathcal{K} = \mathcal{D}$ we obtain

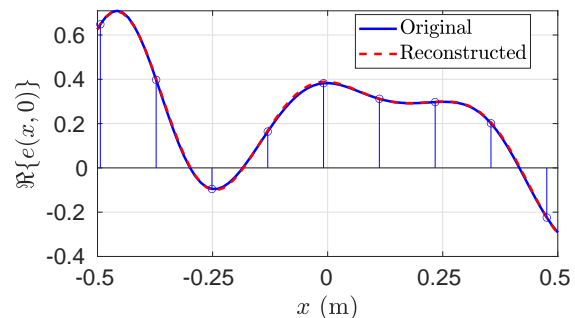
$$f_{\mathcal{D}}(\mathbf{r}) = \frac{|\det(\mathbf{Q}_{\mathcal{D}}^*)|}{(2\pi)^2} \int_{\mathcal{D}} e^{j\mathbf{k}^T \mathbf{r}} d\mathbf{k} \quad (64)$$

$$= \frac{1}{2\sqrt{3}} \int_{\|\mathbf{u}\| \leq 1} e^{j\kappa \mathbf{u}^T \mathbf{r}} d\mathbf{u} \quad (65)$$

where we applied a change of integration variables $\mathbf{u} = \kappa^{-1} \mathbf{I}_2 \mathbf{k} = (u_x, u_y)$ and substituted $|\det(\mathbf{Q}_{\mathcal{D}}^*)| = \lambda^2 / (2\sqrt{3})$ in (33) while using $\kappa = 2\pi/\lambda$. Being (65) an inverse spatial Fourier transform of a rotationally symmetric spectrum, its



(a) $L/\lambda = 20$.



(b) $L/\lambda = 150$.

Fig. 9. Reconstruction of the real part of $e(\mathbf{r})$ from its Nyquist samples under the scattering conditions of Fig. 5b.

result will be invariant under rotation, i.e., $f_{\mathcal{D}}(\mathbf{r}) = f_{\mathcal{D}}(r)$ with $\|\mathbf{r}\| = r$. Hence, we evaluate (65) at the point $\mathbf{r} = (r, 0)$:

$$f_{\mathcal{D}}(\mathbf{r}) = \frac{1}{\sqrt{3}} \int_{-1}^1 e^{j\kappa r u_x} \sqrt{1 - u_x^2} du_x \quad (66)$$

$$\stackrel{(a)}{=} \frac{1}{\sqrt{3}} \int_0^\pi e^{j\kappa r \cos(\theta)} \sin^2(\theta) d\theta \quad (67)$$

where in (a) we applied a change of integration variables $u_x = \cos(\theta)$. By using the Euler's formula and exploiting symmetry of the integrand we obtain

$$f_{\mathcal{D}}(\mathbf{r}) = \frac{\pi}{\sqrt{3}} \frac{J_1(\kappa r)}{\kappa r} = \frac{\pi}{\sqrt{3}} \text{jinc}(\kappa r) \quad (68)$$

where $J_1(\alpha) = \frac{\alpha}{\pi} \int_0^\pi \cos(\alpha \cos(\theta)) \sin^2(\theta) d\theta$ [37, Eq. (9.1.20)].

APPENDIX B

The problem of finding the Nyquist periodicity matrix \mathbf{P}^* for the elliptical embedding of \mathcal{K} is geometrically formulated as an ellipse packing problem, as illustrated in Fig. 4a. Nevertheless, any ellipse can be obtained from a circle by applying an affine mapping $\varphi: \mathcal{D} \rightarrow \mathcal{E}$ defined as $\varphi(\mathbf{k}') = \mathbf{G}^{1/2}\mathbf{k}' = \mathbf{k}$ to every vector $\mathbf{k}' \in \mathcal{D}$. The transformation is sketched in Fig. 4b and is the result of a scaling and counterclockwise rotation by an angle $\phi \in [0, 2\pi]$ of the spatial Cartesian axes:

$$\mathbf{G}^{1/2} = \mathbf{R}\mathbf{D}^{1/2} \quad (69)$$

where $\mathbf{D} = \text{diag}(d_1, d_2) \in \mathbb{R}^{2 \times 2}$ is a diagonal matrix whose entries $0 \leq d_1, d_2 \leq 1$ are the (normalized) lengths of the semi-axes of \mathcal{E} and $\mathbf{R} \in \mathbb{R}^{2 \times 2}$ is a rotation matrix parametrized by the rotation angle ϕ . By virtue of this mapping, the original problem can be turned into a circle packing problem, whose solution is given by $\mathbf{P}_{\mathcal{D}}^*$ in (31). The Nyquist periodicity matrix is then given by

$$\mathbf{P}_{\mathcal{E}}^* = \mathbf{G}^{1/2}\mathbf{P}_{\mathcal{D}}^*. \quad (70)$$

The Nyquist sampling matrix $\mathbf{Q}_{\mathcal{E}}^*$ is computed from (26) as

$$\mathbf{Q}_{\mathcal{E}}^* = (\mathbf{G}^{-1/2})^T \mathbf{Q}_{\mathcal{D}}^* \quad (71)$$

where we expanded the matrix inversion using (70) and substituted the $\mathbf{Q}_{\mathcal{D}}^*$ expression in (32). Here, the inverse transformation matrix is obtainable from (69) as $(\mathbf{G}^{-1/2})^T = \mathbf{R}\mathbf{D}^{-1/2}$.

APPENDIX C

From (30), for a wavenumber support $\mathcal{K} = \mathcal{E}$ we obtain

$$f_{\mathcal{E}}(\mathbf{r}) = \frac{|\det(\mathbf{Q}_{\mathcal{E}}^*)|}{(2\pi)^2} \int_{\mathcal{E}} e^{j\mathbf{k}^T \mathbf{r}} d\mathbf{k} \quad (72)$$

$$= |\det(\mathbf{G}^{1/2})| \frac{|\det(\mathbf{Q}_{\mathcal{D}}^*)|}{(2\pi)^2} \int_{\mathcal{D}} e^{j(\mathbf{G}^{1/2}\mathbf{k}')^T \mathbf{r}} d\mathbf{k}' \quad (73)$$

where we applied the change of integration variables $\mathbf{k}' = \varphi^{-1}(\mathbf{k}) = \mathbf{G}^{-1/2}\mathbf{k}$ with $\mathbf{k}' \in \mathcal{D}$. Based on (36), we rewrite (73) as

$$f_{\mathcal{E}}(\mathbf{r}) = \frac{|\det(\mathbf{Q}_{\mathcal{D}}^*)|}{(2\pi)^2} \int_{\mathcal{D}} e^{j(\mathbf{G}^{1/2}\mathbf{k}')^T \mathbf{r}} d\mathbf{k}'. \quad (74)$$

By re-arranging the terms at the exponential of (74), from (65) we obtain $f_{\mathcal{E}}(\mathbf{r}) = f_{\mathcal{D}}((\mathbf{G}^{1/2})^T \mathbf{r})$. Also, by replacing the transformation matrix $\mathbf{G}^{1/2}$ with its expression in (69) and exploiting the rotation invariance of $f_{\mathcal{D}}(\mathbf{r})$, i.e., $f_{\mathcal{D}}(\mathbf{R}\mathbf{r}) = f_{\mathcal{D}}(\mathbf{r})$ for any rotation matrix \mathbf{R} , we have that $f_{\mathcal{E}}(\mathbf{r}) = f_{\mathcal{D}}(\mathbf{D}^{1/2}\mathbf{r})$.

REFERENCES

- [1] A. Pizzo, T. L. Marzetta, and L. Sanguinetti, "Degrees of Freedom of Holographic MIMO Channels," in *2020 IEEE 21st Int. Workshop Signal Process. Adv. Wireless Commun. (SPAWC)*, 2020, pp. 1–5.
- [2] C. Shannon, "Communication in the presence of noise," *Proceedings of the IRE*, vol. 37, no. 1, pp. 10–21, 1949.
- [3] J. M. Whittaker, "The "Fourier" Theory of the Cardinal Function," *Proceedings of the Edinburgh Mathematical Society*, vol. 1, no. 3, p. 169–176, 1928.
- [4] V. A. Kotel'nikov, *On the Transmission Capacity of the "Ether" and Wire in Electromagnetic Communications*. Boston, MA: Birkhäuser Boston, 2001, pp. 27–45.
- [5] M. Unser, "Sampling-50 years after Shannon," *Proceedings of the IEEE*, vol. 88, no. 4, pp. 569–587, 2000.
- [6] R. Marks, *Introduction to Shannon Sampling and Interpolation Theory*. Springer-Verlag New York, 1991.
- [7] D. E. Dudgeon and R. M. Mersereau, *Multidimensional Digital Signal Processing*. Prentice Hall, 1990.
- [8] D. P. Petersen and D. Middleton, "Sampling and reconstruction of wave-number-limited functions in n-dimensional euclidean spaces," *Information and Control*, vol. 5, no. 4, pp. 279–323, 1962.
- [9] H. Kunsch, E. Agrell, and F. Hamprecht, "Optimal lattices for sampling," *IEEE Trans. Inf. Theory*, vol. 51, no. 2, pp. 634–647, 2005.
- [10] M. D. Migliore, "Horse (electromagnetics) is more important than horse-man (information) for wireless transmission," *IEEE Trans. Antennas Propag.*, vol. 67, no. 4, pp. 2046–2055, 2019.
- [11] A. Pizzo, L. Sanguinetti, and T. L. Marzetta, "Holographic MIMO Communications," *CoRR*, vol. abs/2105.01535, 2021. Online: <https://arxiv.org/abs/2105.01535>.
- [12] S. Hu, F. Rusek, and O. Edfors, "Beyond massive mimo: The potential of data transmission with large intelligent surfaces," *IEEE Trans. Signal Process.*, vol. 66, no. 10, pp. 2746–2758, 2018.
- [13] Q. Wu and R. Zhang, "Intelligent reflecting surface enhanced wireless network via joint active and passive beamforming," *IEEE Trans. Wireless Commun.*, vol. 18, no. 11, pp. 5394–5409, 2019.
- [14] E. Björnson, L. Sanguinetti, H. Wymeersch, J. Hoydis, and T. L. Marzetta, "Massive MIMO is a reality - what is next?: Five promising research directions for antenna arrays," *Digital Signal Processing*, vol. 94, pp. 3 – 20, 2019.
- [15] Q. Wu and R. Zhang, "Towards smart and reconfigurable environment: Intelligent reflecting surface aided wireless network," *IEEE Commun. Mag.*, vol. 58, no. 1, pp. 106–112, 2020.
- [16] W. C. Chew, *Waves and Fields in Inhomogeneous Media*. Wiley-IEEE Press, 1995.
- [17] O. Bucci and G. Franceschetti, "On the spatial bandwidth of scattered fields," *IEEE Trans. Antennas Propag.*, vol. 35, no. 12, pp. 1445–1455, 1987.
- [18] O. Bucci, C. Gennarelli, and C. Savarese, "Representation of electromagnetic fields over arbitrary surfaces by a finite and nonredundant number of samples," *IEEE Trans. Antennas Propag.*, vol. 46, no. 3, pp. 351–359, 1998.
- [19] A. S. Y. Poon, R. W. Brodersen, and D. N. C. Tse, "Degrees of freedom in multiple-antenna channels: a signal space approach," *IEEE Trans. Inf. Theory*, vol. 51, no. 2, pp. 523–536, Feb 2005.
- [20] R. A. Kennedy, P. Sadeghi, T. D. Abhayapala, and H. M. Jones, "Intrinsic limits of dimensionality and richness in random multipath fields," *IEEE Trans. Signal Process.*, vol. 55, no. 6, pp. 2542–2556, 2007.
- [21] L. W. Hanlen and T. D. Abhayapala, "Space-time-frequency degrees of freedom: Fundamental limits for spatial information," in *2007 IEEE Int. Symposium Inf. Theory (ISIT)*, 2007, pp. 701–705.
- [22] A. M. Sayeed, "Deconstructing multiantenna fading channels," *IEEE Trans. Signal Process.*, vol. 50, no. 10, 2002.
- [23] A. Pizzo, L. Sanguinetti, and T. L. Marzetta, "Spatial Characterization of Electromagnetic Random Channels," *CoRR*, vol. abs/2103.15666, 2021. Online: <https://arxiv.org/abs/2103.15666>.
- [24] A. Pizzo, T. L. Marzetta, and L. Sanguinetti, "Spatially-Stationary Model for Holographic MIMO Small-Scale Fading," *IEEE J. Sel. Areas Commun.*, vol. 38, no. 9, pp. 1964–1979, 2020.
- [25] T. L. Marzetta, "Spatially-stationary propagating random field model for Massive MIMO small-scale fading," in *2018 IEEE Int. Symposium Inf. Theory (ISIT)*, June 2018, pp. 391–395.
- [26] T. L. Marzetta, "BLAST Arrays of Polarimetric Antennas," Nokia Proprietary, ITD-01-41984K, 10 05 2001.
- [27] M. Franceschetti, *Wave Theory of Information*. Cambridge University Press, 2017.
- [28] R. Kennedy and T. Abhayapala, "Source-field wave-field concentration and dimension: towards spatial information content," in *2004 IEEE Int. Symposium Inf. Theory (ISIT)*, 2004, pp. 243–.
- [29] M. Franceschetti, "On Landau's eigenvalue theorem and information cut-sets," *IEEE Trans. Inf. Theory*, vol. 61, no. 9, Sept 2015.
- [30] E. Agrell and B. Csébfalvi, "Multidimensional sampling of isotropically bandlimited signals," *IEEE Signal Process. Lett.*, vol. 25, no. 3, pp. 383–387, 2018.
- [31] S. Boyd and L. Vandenberghe, *Convex Optimization*. USA: Cambridge University Press, 2004.
- [32] H. Landau and H. Widom, "Eigenvalue distribution of time and frequency limiting," *Journal of Mathematical Analysis and Applications*, vol. 77, no. 2, pp. 469–481, 1980.
- [33] E. W. Weisstein, "Gauss's Circle Problem," from MathWorld—A Wolfram Web Resource. [Online]. Available: <https://mathworld.wolfram.com/GaussCircleProblem.html>

- [34] T. L. Marzetta, E. G. Larsson, and T. B. Hansen, "Massive MIMO and Beyond," in *Information Theoretic Perspectives on 5G Systems and Beyond*, S. S. I. Maric, O. Simeone, Ed. Cambridge: Cambridge University Press, 2020.
- [35] H. L. Van Trees, *Detection Estimation and Modulation Theory, Part I*. Wiley, 1968.
- [36] A. Paulraj, R. Nabar, and D. Gore, *Introduction to Space-Time Wireless Communications*. Cambridge, UK: Cambridge University Press, 2003.
- [37] M. Abramowitz and I. A. Stegun, Eds., *Handbook of Mathematical Functions with Formulas, Graphs, and Mathematical Tables*. Washington, DC, USA: U.S. Government Printing Office, 1972.